

High Current-Density-Charging Lithium Metal Batteries Enabled by Double-Layer Protected Lithium Metal Anode

Ju-Myung Kim, Mark H. Engelhard, Bingyu Lu, Yaobin Xu, Sha Tan, Bethany E. Matthews, Shalini Tripathi, Xia Cao, Chaojiang Niu, Enyuan Hu, Seong-Min Bak, Chongmin Wang, Ying Shirley Meng, Ji-Guang Zhang,* and Wu Xu*

The practical application of lithium (Li) metal anode (LMA) is still hindered by non-uniformity of solid electrolyte interphase (SEI), formation of “dead” Li, and continuous consumption of electrolyte although LMA has an ultrahigh theoretical specific capacity and a very low electrochemical redox potential. Herein, a facile protection strategy is reported for LMA using a double layer (DL) coating that consists of a polyethylene oxide (PEO)-based bottom layer that is highly stable with LMA and promotes uniform ion flux, and a cross-linked polymer-based top layer that prevents solvation of PEO layer in electrolytes. Li deposited on DL-coated Li (DL@Li) exhibits a smoother surface and much larger size than that deposited on bare Li. The LiF/Li₂O enriched SEI layer generated by the salt decomposition on top of DL@Li further suppresses the side reactions between Li and electrolyte. Driven by the abovementioned advantageous features, the DL@Li||LiNi_{0.6}Mn_{0.2}Co_{0.2}O₂ cells demonstrate capacity retention of 92.4% after 220 cycles at a current density of 2.1 mA cm⁻² (C/2 rate) and stability at a high charging current density of 6.9 mA cm⁻² (1.5 C rate). These results indicate that the DL protection is promising to overcome the rate limitation of LMAs and high energy-density Li metal batteries.

very low electrochemical redox potential (−3.040 V vs standard hydrogen electrode).^[1,2] However, the practical usage of Li metal anode (LMA) is hindered by following challenges: 1) generation of heterogeneous/nonuniform solid electrolyte interphase (SEI) layer,^[3,4] 2) formation of electrochemically inactive or “dead” Li during repeated cycling causing volume change and loss of Li inventory,^[5,6] and 3) continuous consumption of electrolyte triggering low Coulombic efficiency (CE).^[7,8] The seriousness of these challenges increases with increasing the charge current density, thus accelerating the failure of Li metal batteries (LMBs).^[9]

Recently, several protection strategies to address the challenges of LMAs have been developed using a polymeric layer, such as polyvinyl alcohol,^[10] polyvinylidene difluoride (PVDF),^[11] and polyurea.^[12] The composite layers with a mixture of organic/inorganic components were also used to improve ionic transport. These

composite layers include PVDF-co-hexafluoropropylene (PVDF-HFP)/Li fluoride (LiF),^[13] LiF/polytetrafluoroethylene (PTFE),^[14] and LiF/polyethylene oxide (PEO),^[15] LiPEO-ureido-pyrimidinone,^[16] 2,2,3,4,4,4-Hexafluorobutyl acrylate (PHALF)-LiTFSI.^[17] Among the polymer candidates, PEO is well known to be stable


1. Introduction

Lithium (Li) metal has been regarded as one of the most promising anodes to achieve a high energy-density battery due to its ultrahigh theoretical specific capacity (3860 mAh g⁻¹) and

J.-M. Kim, B. E. Matthews, S. Tripathi, X. Cao, C. Niu, J.-G. Zhang, W. Xu

Energy and Environment Directorate
Pacific Northwest National Laboratory
Richland, WA 99354, USA
E-mail: jiguang.zhang@pnnl.gov; wu.xu@pnnl.gov

M. H. Engelhard, Y. Xu, C. Wang
Environmental and Molecular Sciences Laboratory
Pacific Northwest National Laboratory
Richland, WA 99354, USA

 The ORCID identification number(s) for the author(s) of this article can be found under <https://doi.org/10.1002/adfm.202207172>.

© 2022 Battelle Memorial Institute and The Authors. Advanced Functional Materials published by Wiley-VCH GmbH. This is an open access article under the terms of the Creative Commons Attribution License, which permits use, distribution and reproduction in any medium, provided the original work is properly cited.

B. Lu, Y. S. Meng
Department of NanoEngineering
University of California San Diego
La Jolla, CA 92093, USA

S. Tan, E. Hu
Chemistry Division
Brookhaven National Laboratory
Upton, NY 11973, USA

S.-M. Bak
National Synchrotron Light Source II
Brookhaven National Laboratory
Upton, NY 11973, USA

Y. S. Meng
Pritzker School of Molecular Engineering
University of Chicago
Chicago, IL 60637, USA

DOI: 10.1002/adfm.202207172

with Li metal and has a high donor number for Li-ion and high chain flexibility, which are important for promoting ion transport and considered a suitable candidate for an ionic conductive protection layer for LMAs.^[18] Based on this PEO's feature, PEO-based multilayered solid polymer electrolytes to contribute to the stable SEI and cathode electrolyte interphase (CEI) layer were reported.^[19] However, the dissolution or swelling of PEO in liquid electrolytes due to its dimensional instability remains an issue.^[15]

In this study, intrigued by the chemical/structural advantageous features of PEO, a double layer (DL) protection concept is proposed. The DL consists of a PEO-based bottom layer (BL) directly contacting LMA and a cross-linked top layer (TL) coated on the PEO layer. The Li bis(trifluoromethanesulfonyl)imide (LiTFSI) salt is included in the BL to boost the ionic transport inside the protection layer. The TL is a cross-linked polymer composed of phosphoric acid 2-hydroxyethyl methacrylate ester to preserve the mechanical and dimensional stability of the protection layer against liquid electrolytes during cycling. The LMAs using LMAs with and without the DL protection were investigated under different conditions, especially at high current densities that were not reported in most of previous works. The postmortem analyses of both anode and cathode by various microscopic spectroscopies also have been used to reveal the mechanism behind the improved fast charging capabilities of DL-protected LMAs and LMAs.

2. Results and Discussion

2.1. Physicochemical Properties of DL Protection

Although several studies have reported the development of PEO-included protection layers for LMAs,^[15,20,21] there are still concerns about dissolution or swelling of PEO in carbonate or ether solvents-based electrolytes due to the dimensional instability of PEO in these liquid electrolytes. To address this problem, a new concept of DL protection is introduced in this work. The DL layer includes a BL consisting of a PEO layer mixed with selected amount of Li salt, and a TL based on phosphoric acid 2-hydroxyethyl methacrylate ester that is a cross-linkable monomer. The TL material was selected to maintain the mechanical stability of DL in the given electrolyte during electrochemical cycling. An ether-based localized high concentration electrolyte (LHCE), containing Li bis(fluorosulfonyl) imide (LiFSI), 1,2-dimethoxyethane (DME), and 1,1,2,2-tetrafluoroethyl-2,2,3,3-tetrafluoropropyl ether (TTE) at a molar ratio of 1:1.2:3, was used in this work. The stability of PEO in this electrolyte was first evaluated by adding 75 μL electrolyte to a small piece (19 mm diameter) of PEO coated copper (Cu) foil (see Experimental Section for preparation procedure). After 1 h, the PEO layer became swollen and could not preserve its original form when it was scratched out (Figure S1 and Video S1, Supporting Information). In contrast, the DL-coated Cu foil (see Experimental Section for preparation procedure) soaked in the same electrolyte exhibits good physical stability indicating that the TL can prevent the dissolution or swelling of the PEO-based layer against the electrolyte at the same condition (Video S2, Supporting Information).

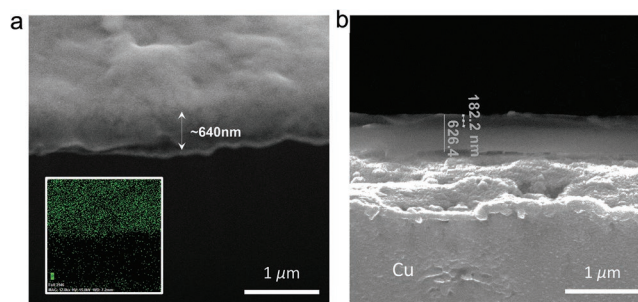


Figure 1. Morphology of DL. a) Cryo-FIB cut cross-sectional DL-3@Li and EDS mapping for P element (inset). b) Cross-sectional SEM image of DL-3@Cu.

The cross-sectional image of the DL-3@Li obtained by cryogenic focused ion beam and scanning electron microscopy (FIB/SEM) in **Figure 1a** indicates that the DL has a thickness of ≈ 640 nm. Also, the TL-containing P is confirmed by the energy-dispersive spectrometry (EDS) mapping through an inset image of **Figure 1a**. To further investigate the respective thickness of TL and BL, the DL-3 coated Cu (DL-3@Cu) was prepared in the same way as DL-3@Li. The DL consists of ≈ 182 nm of TL and ≈ 444 nm of BL and has a total thickness of ≈ 626 nm which is quite similar to the DL on the Li (**Figure 1b**). In addition, the characteristics of the DL can be detected by X-ray photoelectron spectroscopy (XPS) spectra (**Figure S2**, Supporting Information). The DL@Li appears the species of TL such as C–C–O (533.4 eV, O 1s), C=O (531.4 eV, O 1s; 288.5 eV, C 1s), and PO_4 (134.5 eV, P 2p).^[22–24] While the Li residual compounds like LiOH (533.8 eV, O 1s) and Li_2O (531.2 eV, O 1s)^[25] were detected on the bare Li, it is believed that the LMA was a bit exposed to air during sample transfer to the equipment. This result will be revisited later to compare to the one after Li deposition/stripping.

2.2. Electrochemical Stability and Li Deposition Behavior of DL@Li

The long-term cyclability and Li plating/stripping behavior of symmetric cells with the DL- and TL-coated LMAs were further evaluated. As shown in **Figure 2a**, the TL-coated Li (TL@Li) presents a lower overpotential than the DL@Li during cycling. The slightly larger polarization of DL@Li could come from the relatively larger thickness of the DL than that of the TL. The LiTFSI salt was added into the PEO-based BL as an additive to improve the ion transport of the DL. The weight ratio of PEO to LiTFSI (1:x) was changed from $x = 0$ to $x = 3$ and each sample was labeled as DL-x according to the ratio of the LiTFSI (x). DL-3@Li is chosen as the optimal sample because it has the lowest overpotential during cycling of the Li||Li symmetric cells at the current density of 1 mA cm^{-2} for a capacity of 1 mAh cm^{-2} Li deposition as shown in **Figure S3** (Supporting Information). The Li transference numbers of the TL, DL-0, and DL-3 films were measured in the Li||Li symmetric cells (**Figure S4**, Supporting Information). The DL-3 film shows the highest Li transference number of 0.51. These results imply that the LiTFSI salt in the DL could improve Li-ion conducting ability through

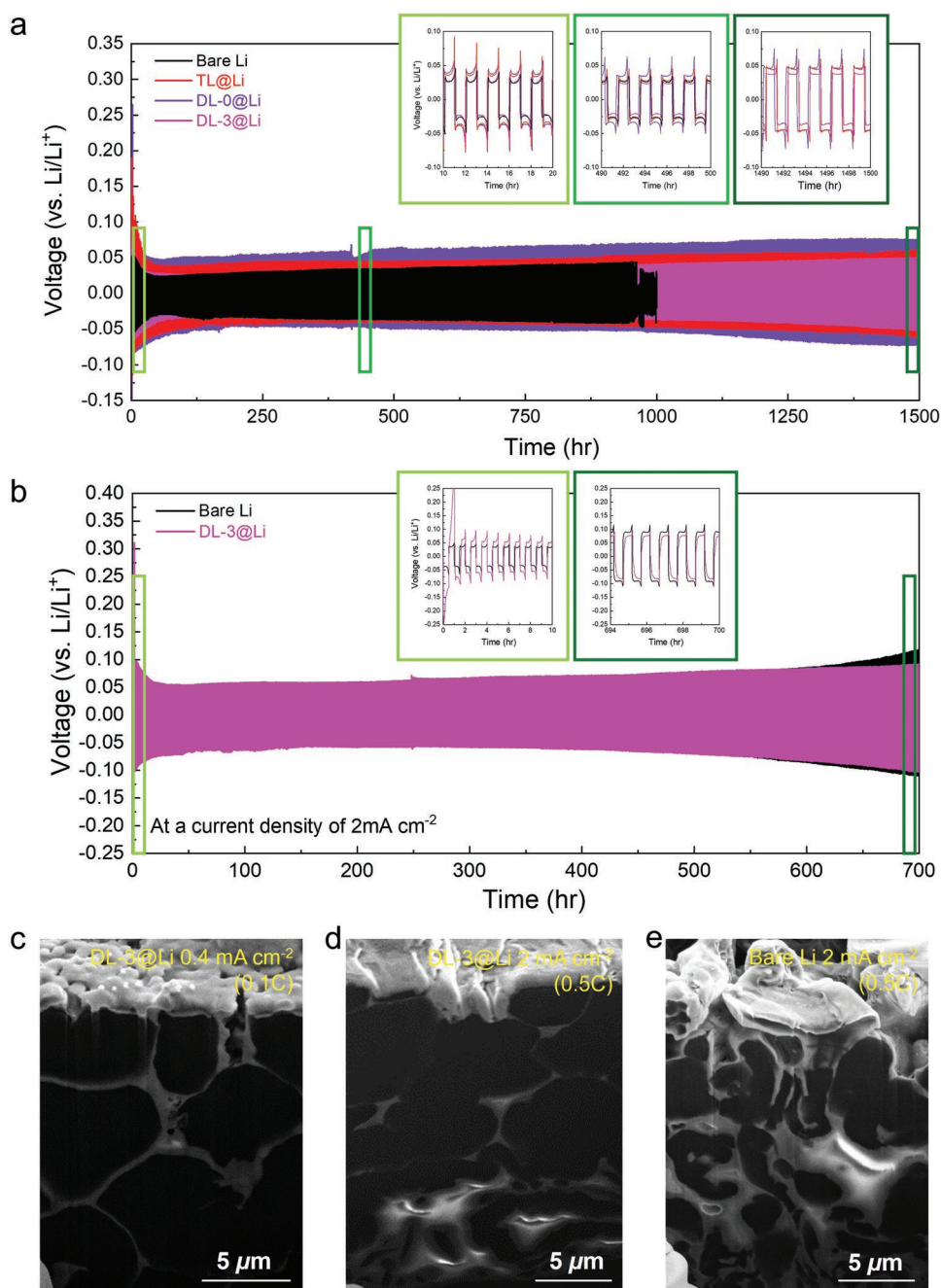


Figure 2. Electrochemical stability and Li deposition behavior of DL@Li. Cycling performance of Li||Li symmetric cells at a current density of a) 1 mA cm^{-2} and b) 2 mA cm^{-2} for a capacity of 1 mAh cm^{-2} . Cryo-FIB cross-sectional images of c) DL-3@Li after Li deposition at a current density of 0.4 mA cm^{-2} for a capacity of 4 mAh cm^{-2} , and d) DL-3@Li and e) bare Li after Li deposition at a current density of 2 mA cm^{-2} for a capacity of 4 mAh cm^{-2} .

the protection layer, which is expected to result in better Li electrodeposition. In addition, the DL-3@Li cell displays a stable Li plating/stripping behavior and maintains the lowest overpotentials in the testing time of 1500 h compared to TL@Li, DL-0@Li, and Bare Li (Figure 2a). In contrast, the bare Li cell fails within 960 h. At the higher current density of 2 mA cm^{-2} , a good cycling stability is obtained on the DL-3@Li up to 700 h without severe overpotentials as shown in Figure 2b. More strikingly, the DL-3@Li could alleviate electrolyte consump-

tion that induces more interface reaction during cycling. The sudden voltage changes observed on the cycling curves of the bare Li as shown in the inset image of Figure 2b could mean continuously building up and breaking down of SEI layers at the electrolyte and Li anode interface.

To explore the Li deposition behavior of both bare Li and DL-3@Li, the Li was deposited at a current density of 0.4 mA cm^{-2} for a capacity of 4 mAh cm^{-2} . The DL-3@Li shows a denser Li layer with bigger Li particles in the cross-sectional

SEM image (Figure 2c) compared to the bare Li (Figure S5, Supporting Information) although the top-view images of both samples exhibit a practically similar size of spherical morphology (Figure S6a,b, Supporting Information). Such a dense Li deposition behavior minimizes the side reactions between Li and electrolyte by the ionic-conductive DL protection. To precisely verify the bright region that covers on the deposited Li in the cross-sectional images, EDS mapping and XPS were measured. EDS mapping images not only underline that DL-3@Li has a larger size of deposited Li particles than the bare Li, but also show that the deposited Li is covered by the layer containing S, F, and O elements (Figure S7a,b, Supporting Information). The XPS surface spectra of both bare Li and DL-3@Li show FSI⁻ anion derived SEI layer as reported in previous studies (Figure S8, Supporting Information).^[26] Interestingly, the SEI layer of DL-3@Li seems to include more of FSI⁻ anion converted components such as LiF (684.7 eV, F 1s), S-F (688.6 eV, F 1s; 169.3 eV, S 2p).^[27] Moreover, not only the F-species in the SEI layer through the depth profiling of the Li deposited DL-3@Li are mainly composed of LiF while the bare Li's SEI layer has LiF and C-F, but also the O-species show a uniform distribution of Li₂O that is assumed the decomposition of LiFSI salt^[28] along with the depth of the DL-3@Li after deposition (Figure S9, Supporting Information). These results suggest that the reaction between Li metal and solvent was relatively suppressed on the surface of the DL-3@Li compared to the bare Li when the Li is deposited. Besides, the LiF and Li₂O enriched SEI layer on the DL-3@Li is believed to be helpful for the enhancement of Li ion diffusion and the mechanical strength of the SEI layer.^[26,29] However, different from the fresh sample (Figure S2, Supporting Information), the characteristic peaks of the TL could not be found on the DL-3@Li after deposition by XPS. Although the presence of the DL was confirmed through P K-edge of the X-ray absorption spectroscopy (Figure S10, Supporting Information) after Li deposition, it is still challenging to exactly elaborate where the Li was deposited. We assume the Li was primarily deposited beneath the DL and some of them could deposit on the top of the DL through the pinholes of the DL layer, but this hypothesis needs to be confirmed in future work.

Driven by the abovementioned advantages of the DL-3@Li, it preserves the denser morphology with the bigger Li particles and smoother surface even after deposition at a current density of 2 mA cm⁻² for a capacity of 4 mAh cm⁻² (Figure 2d; Figures S6c and S7c, Supporting Information). In contrast, the Li particles deposited on bare Li substrate exhibit a porous morphology with a larger amount of SEI layer generation as shown in Figure 2e and Figures S6d and S7d (Supporting Information). It is well known that maintaining the stability of LMAs at high current densities and high capacities is difficult due to uncontrolled interfacial reactions and induced overpotentials that generate byproducts like “dead” Li and undesirable SEI layers.^[30,31] The Li deposition morphology differences imply that the DL-3@Li may give a uniform ion flux with protection against the electrolyte during cycling at a high current density. To further evaluate the stability of DL-3@Li compared to the bare Li, the average CEs of Li deposition/stripping in Li||Cu cells with 75 μL electrolyte were measured as described in the Experimental Section. The DL-3@Li exhibits slightly higher

average CE indicating the protection layer could maintain the LMA stability (Figure S11, Supporting Information).

2.3. Electrochemical Cyclability of Li||LiNi_{0.6}Mn_{0.2}Co_{0.2}O₂ Cells

The long-term cycling performances of Li||LiNi_{0.6}Mn_{0.2}Co_{0.2}O₂ (NMC622) cells with DL-3@Li and bare Li were evaluated at C/10 charging rate and C/3 discharging rate (1C = 4.2 mA cm⁻²) in the voltage range of 2.8 to 4.4 V as shown in Figure S12 (Supporting Information). Both cells show good life span over 400 cycles at slow current densities and DL-3@Li still demonstrates lightly better cycling stability than bare Li. On the other hand, the DL-3@Li||NMC622 cell proves the significant effect of DL-3 protection with the improved cycle life at a charging/discharging rate of C/2 (i.e., 2.1 mA cm⁻²) (Figure 3a) and decreased overpotential after cycling (Figure S13, Supporting Information). Although the DL-3@Li shows a lower initial discharging capacity of 149.0 mAh g⁻¹ than the bare Li (156.7 mAh g⁻¹), the capacity retention (92.4%) was extremely increased compared to the bare Li (36.9%) after 220 cycles. The flatter and smoother surface of the DL-3@Li than the bare Li demonstrates that the DL protection could not only prevent the side reaction between the electrolyte and Li metal during cycling, but also provide uniform ion flux by the ionic conductive characteristics during cycling (Figure 3b). In contrast, the bare Li has a porous and dendritic surface reflecting the drastic capacity decay.

To delve into the beneficial effect of the DL protection for the Li||NMC622 cell, the XPS analysis for the LMAs was performed after 220 cycles. The cycled DL-3@Li (Figure 3c) displays a similar tendency to the one after the first Li deposition (Figure S9a, Supporting Information). Also, it is found that the SEI layer on the DL-3@Li is mainly composed of salt-reduced components such as LiF and Li₂O (Figure S14, Supporting Information). Comparatively, the bare Li shows a relatively higher content of the diluent derived species (C-F) and a lower content of LiF and Li₂O in the SEI components (Figure S14, Supporting Information). However, the high content of S-O_x and N-O_x and the low content of C=O in the SEI on bare Li still indicate that the SEI is more salt derived instead of solvent derived, consistent with our previous finding using the same electrolyte.^[26] These results emphasize that the DL protection could suppress the constant consumption of the electrolyte by the side reaction and the formation of the unstable SEI layer on dendritic Li. In addition, the uniformity of ion flux and consumption of the electrolyte on the Li anode might affect the cathode side. After 220 cycles, the NMC622 particle from the DL-3@Li cell (Figure S15b, Supporting Information) maintains similar structure to the fresh NMC622 (Figure S15a, Supporting Information) without cracks as obtained through the FIB-SEM images. However, the NMC622 from the bare Li cell shows a little crack inside particles (Figure S15c, Supporting Information). These structural differences are also observed from the scanning transmission electron microscope (STEM) analysis. Although NMC622 cathodes present the same thickness of the cation mixing layer, a thinner cathode electrolyte interphase (CEI) layer is found on the NMC622 from the DL-3@Li cell compared to the one from the bare Li cell as shown

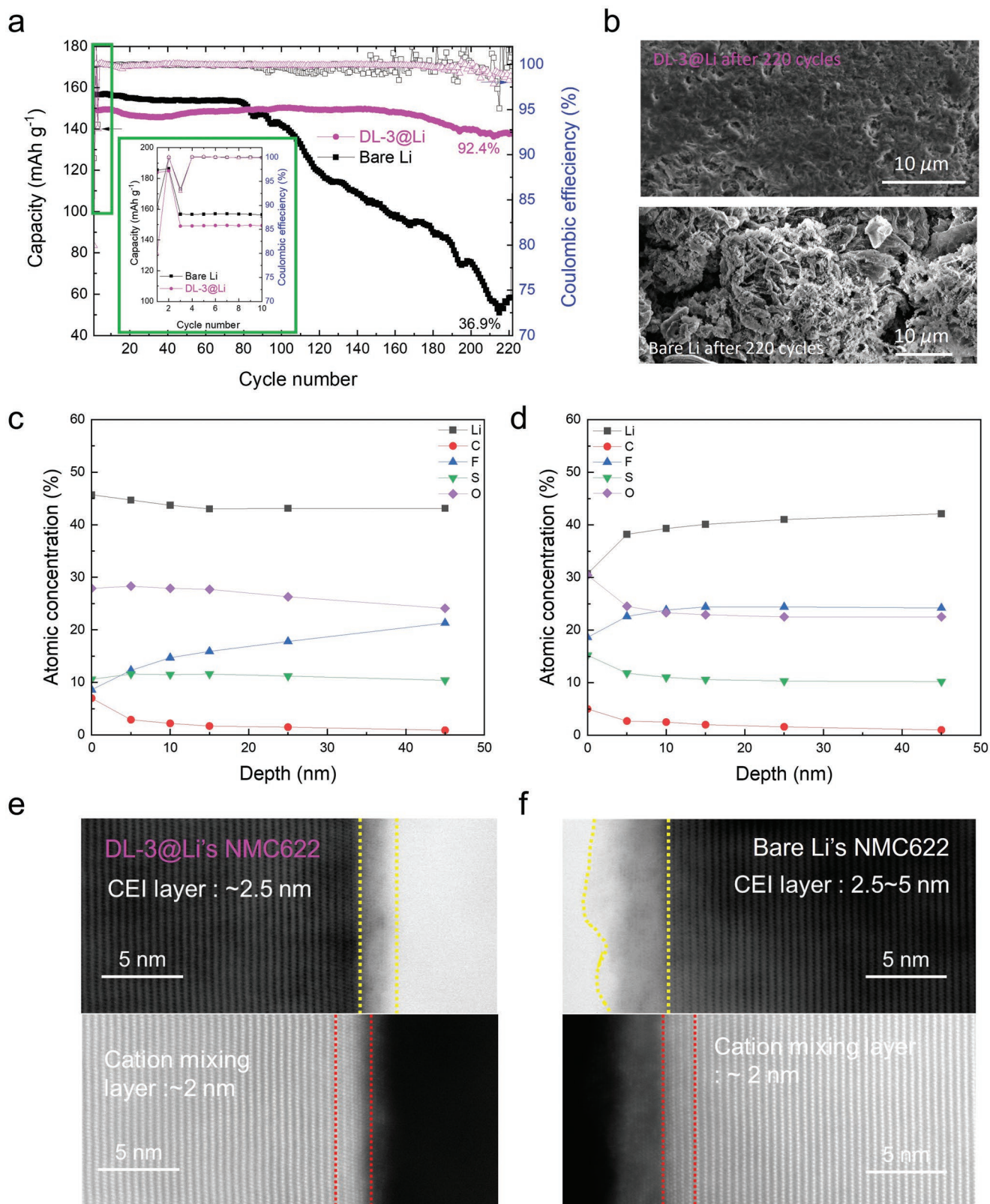


Figure 3. Electrochemical cyclability of Li||LiNi_{0.6}Mn_{0.2}Co_{0.2}O₂ cells. a) Cycling performance of Li||NMC622 cells at a charge/discharge rate of C/2 (IC = 4.2 mA cm⁻²) using DL-3@Li and bare Li. b) Surface SEM images of DL-3@Li and bare Li after 220 cycles. Atomic composition ratios of the SEI quantified by XPS measurement at different depths after 220 cycles for c) DL-3@Li and d) bare Li. Atomic resolution STEM-bright field (BF, top) and high-angle annular dark-field (HAADF, bottom) images after 220 cycles for e) NMC622 paired with DL@Li and f) NMC622 paired with bare Li.

in Figure 3e,f, respectively. It is believed that the surface stability of the DL-3@Li anode by the ionic conductive protection reduces the possibility of generation of radicals on Li surface, thus decreases the crosstalk of the reduced species (mostly radicals)^[32,33] from anode to cathode and alleviates the side reactions of these reduced species to the NMC622 cathode, then enhances the battery life even at a high current density. Notably, the cycling performance of DL-3@Li||NMC622 cells far exceeds those of previously reported Li protection strategies even at the highest areal capacity (Table S1, Supporting Information).

The fast-charging capability of the battery has been considered as one of the crucial requirements, especially for the electric vehicles. We investigated the charge rate capability of Li||NMC622 cells in which the charge current densities varied from C/10 to 1.5C (1C = 4.6 mA cm⁻²) under a constant discharge current density of C/10 (Figure 4a). Based on the highly developed surface of the protection layer that provides uniform ion flux, the DL-3@Li shows an improved charge rate capability than the bare Li. The DL-3@Li cell delivers a higher

discharge capacity of 126.0 mAh g⁻¹ with a lower polarization after charging at 1.5C than the bare Li cell (94.3 mAh g⁻¹) (Figure S16, Supporting Information). To further verify the enhanced ion transport at a high current density, a galvanostatic intermittent titration technique (GITT) analysis was conducted. Figure 4b exhibits that the DL-3@Li suppresses the increase of cell overpotential upon the repeated current stimuli (applied at a current density of 6.9 mA cm⁻², i.e., 1.5C rate), with an interruption time of 2 h between pulses), from which the obtained internal cell resistances are presented as a function of the state of charge (inset image of Figure 4b). In addition, the DL-3@Li displays a smoother deposited surface after charging at a current density of 1.5C (at the step pointed by a green star in Figure 4a), unlike the bare Li that shows a porous morphology (Figure 4c,d). Particularly, the DL-3@Li has no obvious interface between fresh and deposited Li as depicted in the cross-sectional SEM image (Figure 4c). On the other hand, the bare Li presents a huge volume expansion with the interfacial crack indicating the lack of utilization of Li during charging

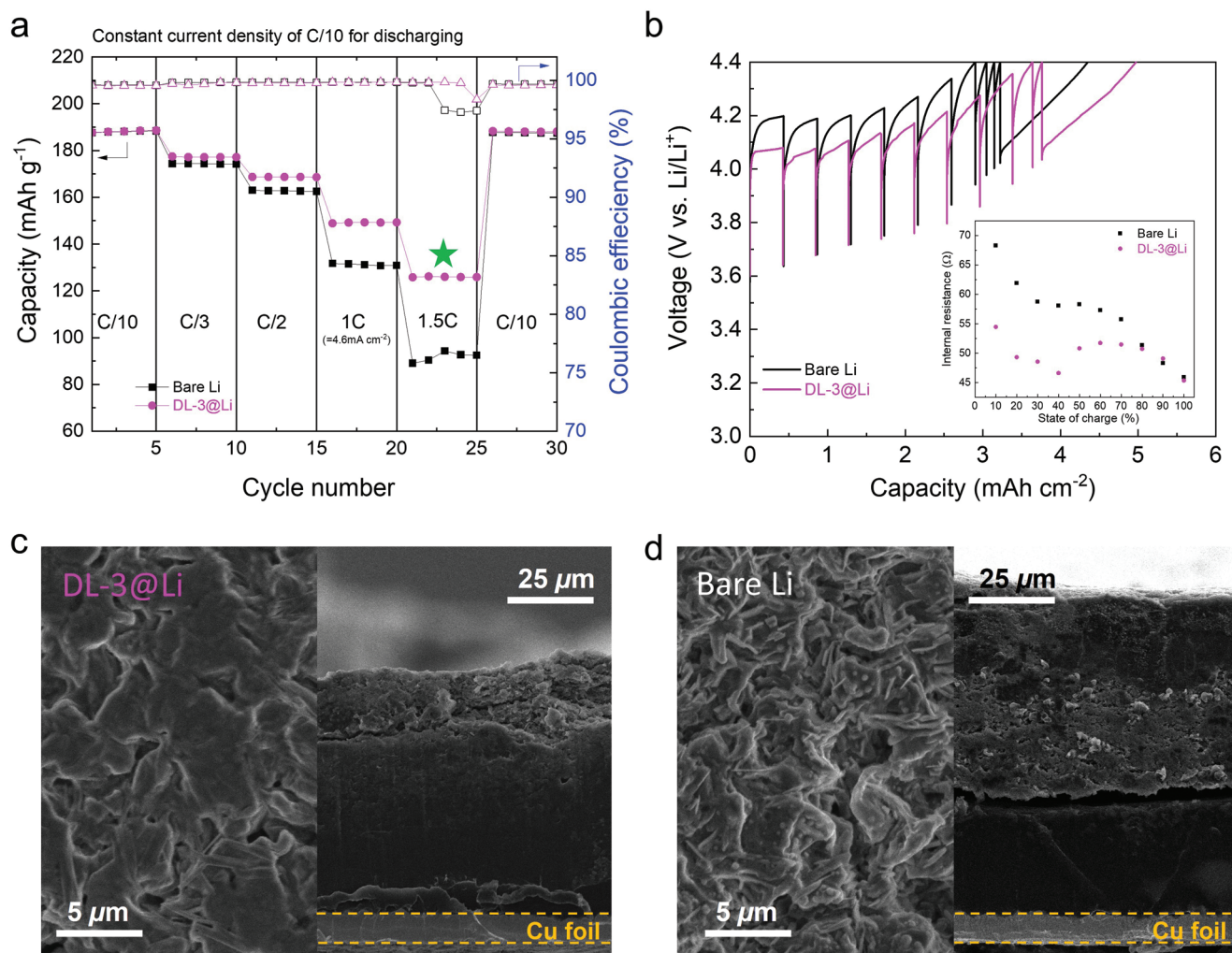
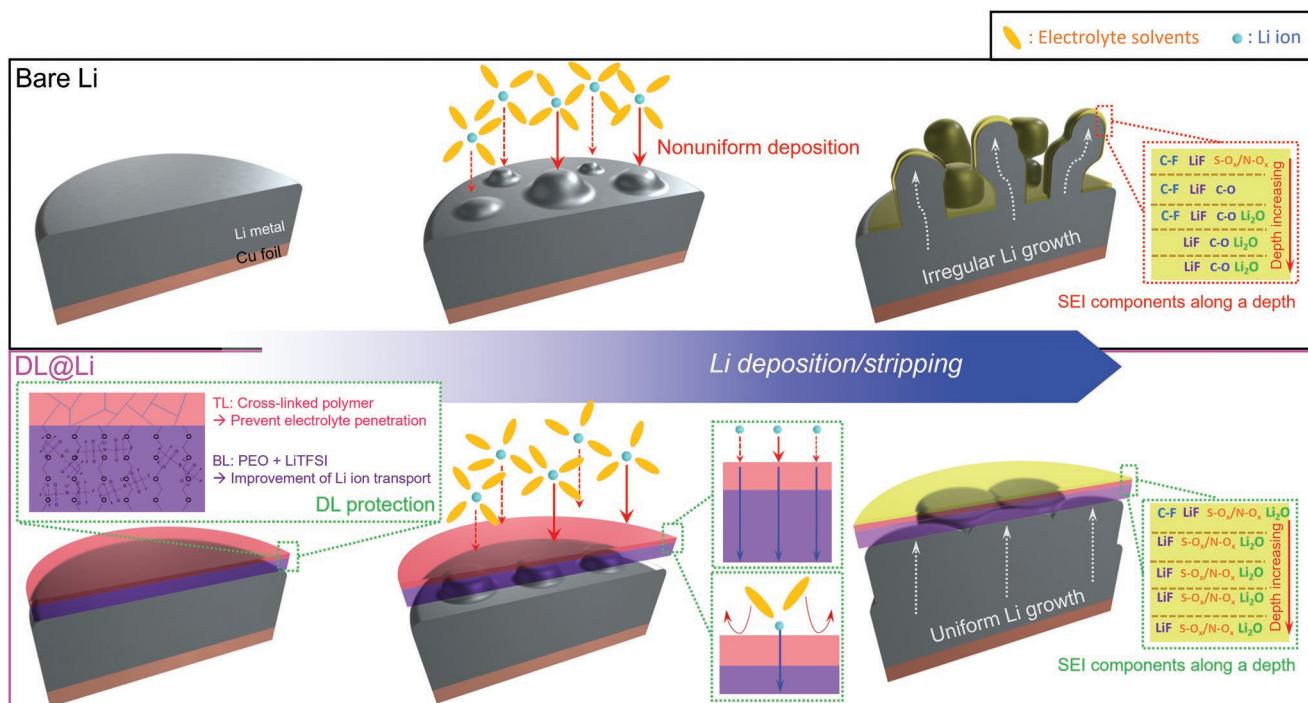


Figure 4. Fast charging capability of Li||LiNi_{0.6}Mn_{0.2}Co_{0.2}O₂ cells. a) Charge rate capability of Li||NMC622 cells using DL-3@Li and bare Li at the charge rates varied from C/10 to 1.5C (1C = 4.6 mA cm⁻²) under a constant discharge rate of C/10. b) GITT profiles of DL-3@Li and bare Li obtained upon the repeated current stimuli (at 1.5C rate or a current density of 6.9 mA cm⁻²), where the interruption time between the pulses = 2 h. Surface and cross-sectional SEM images of c) DL-3@Li and d) bare Li after Li deposition at 1.5C (corresponding to point by a green star in Figure 4a).



Scheme 1. The advantageous effects of DL@Li on supplying uniform Li ion flux, preventing electrolyte penetration, and maintaining SEI composition after Li deposition.

(Figure 4d). These results demonstrate the strategy of the well-developed ionic conductive protection, eventually providing the possibility of superior fast-charging LMBs. The schematic illustration (**Scheme 1**) shows the advantage roles of the DL-3@Li with particular attention paid to the uniform ion flux and suppression of the side reactions.

3. Conclusion

We introduced a DL strategy to protect LMA and improve the electrochemical performance of LMBs. The DL consists of the PEO-based BL that provides uniform ion transport and the cross-linked TL that maintains the mechanical integrity of DL and decreases the side reactions between Li metal and liquid electrolyte. Consequently, the DL@Li allows the formation of a stable SEI layer that is mainly composed of LiF and Li₂O through the prevention of the penetration of electrolytes. In addition, the DL@Li exhibits a smoother surface with bigger particles of Li than the bare Li after deposition. Driven by the physicochemical feature of the DL, the DL@Li||NMC622 cells show superior cyclability with a capacity retention of 92.4% after 220 cycles at a current density of 2.1 mA cm⁻² (C/2 rate) with a smoother surface of the LMA and well-preserved NMC622 cathode structure. Notably, the DL@Li||NMC622 cells achieve a higher discharge capacity of 126.0 mAh g⁻¹ after charging at a high current density of 6.9 mA cm⁻² (1.5C rate) due to the uniform ion flux and reduced side reactions. To the best of our knowledge, such an exceptional electrochemical performance of the DL protection strategy proposed herein has not been reported in the high areal-capacity-loading Li||NMC622

batteries. We believe that such tailored DL protection could be an effective solution to the formidable challenges of high-rate and high-energy-density LMBs.

4. Experimental Section

Preparation of DL@Li: The DL@Li was prepared inside an argon-filled glovebox (moisture and oxygen content ≤ 0.1 ppm) according to the following procedures. Phosphoric acid 2-hydroxyethyl methacrylate (2 wt.%) (PAHEMA, Sigma-Aldrich) and initiator (2-hydroxy-2-methylpropiophenone, HMPP, Sigma-Aldrich) were put in the tetrahydrofuran (THF, anhydrous, $\geq 99.9\%$) solvent and mechanically stirred to make a homogeneous solution for the TL. 1 wt.% of PEO (MW 300,000, Sigma-Aldrich) was put in the N-methyl-pyrrolidone (NMP, anhydrous, 99.5%) solvent and mechanically stirred at 80 °C until PEO was entirely dissolved. After the solution was cooled to room temperature, THF solvent (at NMP:THF = 2:8 by wt.) was added to the PEO solution. In this step, pre-dried LiTFSI (99.95%, Sigma-Aldrich) was added to improve the ionic conductivity of the PEO-based BL. A 50 μm thick Li metal disk was soaked in the PEO solution for 1 min during a dip coating process and dried to evaporate the NMP/THF solvents under vacuum. After that, the PEO-coated Li metal was soaked in the PAHEMA solution to coat the top layer. After the THF solvent was evaporated from the Li surface, the DL@Li was transferred to a UV cross-linker machine (DR-301C, MelodySusie) to cross-link the TL for 5 min. The cross-linked DL@Li was dried under vacuum overnight.

Electrochemical Characterization of DL@Li: To check the electrochemical performance, CR2032 coin cell kits (MTI corporation) with Al-clad positive cases were used to assemble the testing cells in an argon-filled glovebox (MBraun, moisture and oxygen content ≤ 0.1 ppm) using the 4.2–4.6 mAh cm⁻² NMC622 cathode (NMC622 : Carbon black : PVDF binder = 96 : 2 : 2 by wt.%) disks (1.27 cm diameter), the 20 μm thick polyethylene (PE) separator, the obtained DL@Li (1.60 cm diameter) and 75 μL electrolyte (LiFSI (battery grade, Nippon Shokubai), DME (battery grade,

Gotion, Inc.), and TTE (99%, SynQuest), at 1.0:1.2:3.0 by mol). An extra piece of Al foil (1.90 cm diameter) was added in between the NMC622 disk and the Al-clad positive case to avoid the electrolyte corrosion to the stainless steel of the positive case. For the symmetric cells, two DL@Li disks were used as working and counter electrodes, and the stainless-steel case was used as the positive case. Li||NMC622 cells (N/P ratio = 2.2–2.4) were cycled on Landt battery testers at C/2 charge and C/2 discharge after the formation step of two charge/discharge cycles at C/10 in the voltage range of 2.8–4.4 V at 25 °C, where 1C = 4.2–4.6 mA cm⁻². Li||Li symmetric cells were cycled at 2 mA cm⁻² deposition and 2 mA cm⁻² stripping at 25 °C, for a capacity of 1 mAh cm⁻². The Li ion transference number of each polymer film was evaluated using a potentiostatic polarization method with the addition of the liquid electrolyte used in this study.^[34] In the case of the fast-charging test of Li||NMC622 cells, the formation step was the same as that used in cycling test cells, while the constant current density of C/10 was used for discharging and the charging current densities were at C/10, C/3, C/2, 1C, 1.5C, and C/10 for 5 cycles during each charging rate. The GITT profiles were obtained using a potentiostat/galvanostat (VSP classic, Bio Logic).

Structural/Physicochemical Characterizations: The cross-sectional images of the LMAs after deposition were observed by cryogenic Scios FIB-SEM. The surface and cross-sectional images of LMAs after cycling were characterized using SEM. The cross-sectional images of NMC622 particles were obtained by Helios FIB-SEM. For the STEM, samples were prepared using FIB lift out procedures after ≈2 μm Pt layer was deposited on the surface for protection. XPS was carried out on a Physical Electronics Quantera scanning X-ray microprobe, and the obtained spectra were fitted with the CasaXPS software and the binding energy was calibrated with C 1s at 284.8 eV. All the cycled samples were washed with anhydrous DME after disassembling the cells for post analyses. To understand the presence of DL, the P K-edge XAS measurement was performed. The DL@Li samples before and after Li deposition at a current density of 0.4 mA cm⁻² for a capacity of 4 mAh cm⁻² were tested. They were sealed inside the Kapton tape and Mylar film, and then measured in fluorescence mode at 8-BM beamline (TES) of National Synchrotron Light Source II (II) in Brookhaven National Laboratory. The data were analyzed using the Athena software.^[35]

Supporting Information

Supporting Information is available from the Wiley Online Library or from the author.

Acknowledgements

This work was supported by the Assistant Secretary for Energy Efficiency and Renewable Energy, Vehicle Technologies Office of the U.S. Department of Energy (DOE) through the Advanced Battery Materials Research (BMR) program (Battery500 Consortium) under the contract no. DE-AC05-76RL01830 for Pacific Northwest National Laboratory (PNNL) and the contract no. DE-SC0012704 for Brookhaven National Laboratory (BNL). The XPS measurement was supported under a partial grant from the Washington State Department of Commerce's Clean Energy Fund. The microscopic and spectroscopic characterizations were conducted in the William R. Wiley Environmental Molecular Sciences Laboratory (EMSL), a national scientific user facility sponsored by DOE's Office of Biological and Environmental Research and located at PNNL. Cryo-FIB/SEM was performed at the San Diego Nanotechnology Infrastructure (SDNI), a member of the National Nanotechnology Coordinated Infrastructure, which is supported by the National Science Foundation (grant ECCS-1542148). PNNL is operated by Battelle for the DOE under Contract DE-AC05-76RL01830. This research used beamline 8-BM (TES) of the National Synchrotron Light Source II, U.S. DOE Office of Science User Facilities operated for the DOE Office of Science by BNL under Contract No. DE-SC0012704. The salt LiFSI was provided by Dr. Kazuhiko Murata of Nippon Shokubai Co., Ltd.

Conflict of Interest

The authors declare no conflict of interest.

Data Availability Statement

The data that support the findings of this study are available from the corresponding author upon reasonable request.

Keywords

fast charging, high-energy density batteries, lithium metal anodes, lithium metal batteries, protection layers

Received: June 23, 2022

Revised: September 1, 2022

Published online:

- [1] X.-B. Cheng, R. Zhang, C.-Z. Zhao, Q. Zhang, *Chem. Rev.* **2017**, *117*, 10403.
- [2] Y. Zhang, T.-T. Zuo, J. Popovic, K. Lim, Y.-X. Yin, J. Maier, Y.-G. Guo, *Mater. Today* **2020**, *33*, 56.
- [3] P. Zhai, L. Liu, X. Gu, T. Wang, Y. Gong, *Adv. Energy Mater.* **2020**, *10*, 2001257.
- [4] Y. Liu, Y. Cui, *Joule* **2017**, *1*, 649.
- [5] P. Shi, X. Q. Zhang, X. Shen, R. Zhang, H. Liu, Q. Zhang, *Adv. Mater. Technol.* **2020**, *5*, 1900806.
- [6] J. Xiao, *Science* **2019**, *366*, 426.
- [7] R. Xu, X.-B. Cheng, C. Yan, X.-Q. Zhang, Y. Xiao, C.-Z. Zhao, J.-Q. Huang, Q. Zhang, *Matter* **2019**, *1*, 317.
- [8] B. Horstmann, J. Shi, R. Amine, M. Werres, X. He, H. Jia, F. Hausen, I. Cekic-Laskovic, S. Wiemers-Meyer, J. Lopez, *Energy Environ. Sci.* **2021**, *14*, 5289.
- [9] Y. Liu, Y. Zhu, Y. Cui, *Nat. Energy* **2019**, *4*, 540.
- [10] Y. Zhao, D. Wang, Y. Gao, T. Chen, Q. Huang, D. Wang, *Nano Energy* **2019**, *64*, 103893.
- [11] J. Luo, C. C. Fang, N. L. Wu, *Adv. Energy Mater.* **2018**, *8*, 1701482.
- [12] Y. Sun, Y. Zhao, J. Wang, J. Liang, C. Wang, Q. Sun, X. Lin, K. R. Adair, J. Luo, D. Wang, *Adv. Mater.* **2019**, *31*, 1806541.
- [13] R. Xu, X. Q. Zhang, X. B. Cheng, H. J. Peng, C. Z. Zhao, C. Yan, J. Q. Huang, *Adv. Funct. Mater.* **2018**, *28*, 1705838.
- [14] S. Sun, S. Myung, G. Kim, D. Lee, H. Son, M. Jang, E. Park, B. Son, Y.-G. Jung, U. Paik, *J. Mater. Chem. A* **2020**, *8*, 17229.
- [15] C. Fu, C. Battaglia, *ACS Appl. Mater. Interfaces* **2020**, *12*, 41620.
- [16] G. Wang, C. Chen, Y. Chen, X. Kang, C. Yang, F. Wang, Y. Liu, X. Xiong, *Angew. Chem.* **2020**, *132*, 2071.
- [17] S.-M. Xu, H. Duan, J.-L. Shi, T.-T. Zuo, X.-C. Hu, S.-Y. Lang, M. Yan, J.-Y. Liang, Y.-G. Yang, Q.-H. Kong, X. Zhang, Y.-G. Guo, *Nano Res.* **2020**, *13*, 430.
- [18] Z. Xue, D. He, X. Xie, *J. Mater. Chem. A* **2015**, *3*, 19218.
- [19] C. Wang, T. Wang, L. Wang, Z. Hu, Z. Cui, J. Li, S. Dong, X. Zhou, G. Cui, *Adv. Sci.* **2019**, *6*, 1901036.
- [20] G. Li, Z. Liu, D. Wang, X. He, S. Liu, Y. Gao, A. AlZahrani, S. H. Kim, L. Q. Chen, D. Wang, *Adv. Energy Mater.* **2019**, *9*, 1900704.
- [21] G. Wang, C. Chen, Y. Chen, X. Kang, C. Yang, F. Wang, Y. Liu, X. Xiong, *Angew. Chem.* **2020**, *132*, 2071.
- [22] M. A. Khan, M. M. Hassan, L. T. Drzal, *Compos. Part A Appl. Sci. Manuf.* **2005**, *36*, 71.
- [23] A. Thøgersen, J. H. Selj, E. S. Marstein, *J. Electrochem. Soc.* **2012**, *159*, D276.

- [24] W. Luo, D. Y. Zemlyanov, C. A. Milligan, Y. Du, L. Yang, Y. Wu, D. Y. Peide, *Nanotechnology* **2016**, *27*, 434002.
- [25] K. N. Wood, G. Teeter, *ACS Appl. Energy Mater.* **2018**, *1*, 4493.
- [26] X. Ren, L. Zou, X. Cao, M. H. Engelhard, W. Liu, S. D. Burton, H. Lee, C. Niu, B. E. Matthews, Z. Zhu, C. Wang, B. W. Arey, J. Xiao, J. Liu, J.-G. Zhang, W. Xu, *Joule* **2019**, *3*, 1662.
- [27] C. Shen, H. Yan, J. Gu, Y. Gao, J. Yang, K. Xie, *Front. Chem.* **2018**, *6*, 517.
- [28] G. G. Eshetu, X. Judez, C. Li, M. Martinez-Ibañez, I. Gracia, O. Bondarchuk, J. Carrasco, L. M. Rodriguez-Martinez, H. Zhang, M. Armand, *J. Am. Chem. Soc.* **2018**, *140*, 9921.
- [29] R. Guo, B. M. Gallant, *Chem. Mater.* **2020**, *32*, 5525.
- [30] J. Liang, X. Li, Y. Zhao, L. V. Goncharova, G. Wang, K. R. Adair, C. Wang, R. Li, Y. Zhu, Y. Qian, *Adv. Mater.* **2018**, *30*, 1804684.
- [31] G. Jiang, K. Li, F. Yu, X. Li, J. Mao, W. Jiang, F. Sun, B. Dai, Y. Li, *Adv. Energy Mater.* **2021**, *11*, 2003496.
- [32] H. Lee, H.-S. Lim, X. Ren, L. Yu, M. H. Engelhard, K. S. Han, J. Lee, H.-T. Kim, J. Xiao, J. Liu, W. Xu, J.-G. Zhang, *ACS Energy Lett.* **2018**, *3*, 2921.
- [33] J. Langdon, A. Manthiram, *Adv. Funct. Mater.* **2021**, *31*, 2010267.
- [34] S. K. Cho, H. I. Kim, J. W. An, K. Jung, H. Bae, J. H. Kim, T. Yim, S. Y. Lee, *Adv. Funct. Mater.* **2020**, *30*, 2000792.
- [35] B. Ravel, M. Newville, *J. Synchrotron Radiat.* **2005**, *12*, 537.